New Assembly Method for Cellulose Derived Graphene Quantum Dots-Sensitized Solar Cells

Savisha Mahalingam
Universiti Tenaga Nasional
Kam Sheng Lau
National University of Malaysia
Azimah Omar
University of Malaya
Abreeza Manap (Abreeza@uniten.edu.my)
Universiti Tenaga Nasional
Puvaneswaran Chelvanathan
National University of Malaysia
Chin Hua Chia
National University of Malaysia
Nowshad Amin
Universiti Tenaga Nasional
Illona Juliana Mathews
Universiti Tenaga Nasional
Nurfanizan Afandi
Universiti Tenaga Nasional
Nasrudin Abd Rahim
University of Malaya

Research Article

Keywords: Absorption, affinity, dye-sensitized solar cell, graphene quantum dot

Posted Date: February 26th, 2021

DOI: https://doi.org/10.21203/rs.3.rs-242899/v1

New Assembly Method for Cellulose Derived Graphene Quantum Dots-Sensitized Solar Cells

Mahalingam, Savisha[1*], Lau, Kam Sheng[2], Omar, Azimah[3], Manap, Abreeza[1,4], Chelvanathan, Puvaneswaran[5,6], Chia, Chin Hua[2], Amin, Nowshad[1], Mathews, Illona Juliana[4], Afandi, Nurfanizan[4], Abd Rahim, Nasrudin[3,7]

[1]Institute of Sustainable Energy, Universiti Tenaga Nasional, Jalan IKRAM-UNITEN, 43000 Kajang, Selangor, Malaysia
[2]Materials Science Program, Department of Applied Physics, Faculty of Science and Technology, Universiti Kebangsaan Malaysia, 43600 Bangi, Selangor, Malaysia
[3]Higher Institution Centre of Excellence (HICoE), UM Power Energy Dedicated Advanced Centre (UMPEDAC), Level 4, Wisma R&D, University of Malaya, Jalan Pantai Baharu, 59990 Kuala Lumpur, Malaysia
[4]Department of Mechanical Engineering, College of Engineering, Universiti Tenaga Nasional, Jalan IKRAM-UNITEN, 43000 Kajang, Selangor, Malaysia
[5]Solar Energy Research Institute, Universiti Kebangsaan Malaysia, 43600, Bangi, Selangor, Malaysia
[6]Graphene & Advanced 2D Materials Research Group (GAMRG), School of Science and Technology (SST), Sunway University, No. 5, Jalan Universiti, 47500 Bandar Sunway, Selangor, Malaysia
[7]Renewable Energy Research Group, King Abdulaziz University, Jeddah 21589, Saudi Arabia

* Corresponding author: Abreeza@uniten.edu.my

Abstract

Unambiguously layer by layer (LBL) assembly of graphene quantum dots (GQDs) and dye (GQDs/dye) on TiO_2 photoanode is the traditional and straightforward approach in the fabrication of graphene quantum dot-sensitized solar cells (QDSSCs). Unfortunately, limited light absorption and low affinity of GQDs to TiO_2 surface shadow the advantages of LBL and constrains its practical application. Herein, a new strategy of mixture configuration (GQDs+dye) was investigated. A distinctive nanoporous honeycomb hexagonal carbon network of GQDs was found with fewer defects single crystalline structure, and an average size of 9.87 nm was produced from cellulose. Experimental results demonstrated that LBL exhibited the highest efficiency of 16.76 % under low illumination but a lower efficiency (1.43%) than the mixture method (2.91%) under standard light. The increased J_{sc} (5.075 mA/cm^2) and high charge collection efficiency (0.96) in the mixture sample indicated enhanced electron collection at TiO_2. The less -OH groups on TiO_2 provides a good surface intact of GQDs and N719. In addition to that, the high surface potential (33.47 mV) of the premixed sample restricted the photogenerated electrons to go into a deep state, reducing back electron transfer. Therefore, mixture assembly of co-sensitization is an effective approach for light-harvesting in QDSSC.

Keywords: Absorption; affinity; dye-sensitized solar cell; graphene quantum dot

1. Introduction

Pollution and energy demand have been increasing in the past years. To fulfill these incredibly high energy demands, renewable energy such as wind, biomass, and solar energy is introduced. As compared to other renewable energy sources, solar energy has proved to be extremely beneficial to both the environment and the economy. There are several types of solar cells, i.e., silicon solar cells, dye-sensitized solar cells (DSSCs), quantum dot solar cells, perovskite solar cells, and many more [1-3]. Among these solar cells, the conventional silicon solar cell has been widely used commercially due to its longer life and good efficiency. However, the drawback of silicon solar cells is the high manufacturing cost. It is at a great risk of losing its efficiency at higher temperatures (hot sunny days) and limiting its capabilities [3].

A great effort has been made in developing third-generation solar cells as they are manufactured at a low cost, has a more straightforward fabrication method, possesses a moderate efficiency, and has a remarkable ability to perform during cloudy days [4-7]. DSSC can potentially replace the conventional silicon solar cell mainly because the dye acts as a photon collector, while the semiconducting nanomaterial acts as the electron transport carrier. Unlike the conventional silicon solar cell, the silicon acts as both the photon collector and electron transport carrier. However, the downfall of DSSC is its narrow absorption of the solar spectrum, having high charge recombination and low electron injection efficiency. Therefore, charge recombination should be reduced to increase the electron injection efficiency [8].

To enhance conversion efficiency, the photoanode of a solar cell can be modified by adding carbon nanostructure. Graphene, a type of carbon nanostructure material, would be the preferred material used because of its excellent characteristics. However, the disadvantage of using only graphene is its characteristic of having a zero-band gap. Hence, graphene quantum dots (GQDs) are introduced due to its properties that include having a non-zero band gap, being non-toxic, and having stable photoluminescence (PL), good solubility, and most importantly, its ability to tune the bandgap. Typically, GQDs are synthesized via oxidative cutting of carbonic precursors using strong oxidizing agents, such as concentrated sulfuric acid (H_2SO_4) and nitric acid (HNO_3) at harsh conditions [9, 10]. Researchers used both bottom-up [11,12] and top-down [13,14] approaches. For instance, Pan et al. used the top-down method by hydrothermally oxidizing graphene sheets in H_2SO_4 and HNO_3 [15]. Meanwhile, Umrao et al. presented a bottom-up strategy by carbonizing acetylacetone under microwave irradiation [12].

Although these approaches produce size controllable GQDs, few drawbacks limit the development and applications of GQDs. These methods are toxic to the environment as strong oxidizing agents or organic solvents are required as well as the expensive raw materials like carbon-based materials (graphite, graphene, and CNTs) are hardly obtained. Moreover, the purification process to remove the acid residues and/or metallic ions are time-consuming, which indirectly increases the cost. Thus, a green production of GQDs is favorable to increase its application in photovoltaic (PV). Chen et al. reported a green synthesis of GQDs from cellulose, an abundantly available renewable natural resource [16]. The work is composed of cellulose and water with the absence of harmful potent oxidizing agents. The reaction includes hydrolyzation of cellulose to glucose and followed by ring-closure condensation of glucose to GQDs.

GQDs have been employed in PV cells since 2010 as potential electron donors [17] and light absorbers [18]. Researchers added GQDs in all the main compartments of DSSC which are in photoelectrodes [19], light absorbers/sensitizers [18, 20-29], electrolyte [30] and counter electrode [31- 36]. Most researchers have used GQDs as light absorbers co-sensitized with various dyes, such as N719, N3, and D719 in quantum dot-sensitized solar cells (QDSSCs), which are analogous to DSSCs [22-26]. The highest reported efficiency to date utilizing GQDs-sensitized solar cell is around 11 % [24]. This approach follows the type-II alignment where the GQDs is placed in between the TiO_2 and dye (GQDs/dye (layer by layer (LBL))) [37]. The dye plays dual roles where it accepts photons from the Sun and accepts the positively charged holes from HOMO of GQDs which acts as the donor and reduces the internal recombination in the cell. Therefore, GQDs assist in charge separation and collection where more electrons can be injected into the semiconducting oxide without recombining back into the dye hole. This event typically follows the type-II alignment, restricting the injected electron to recombine with the redox electrolyte [23]. Figure 1 shows the type-II alignment of GQDs and dye in QDSSC, where CB and VB represent conduction and valence bands, respectively. However, the potential use of GQDs cannot be fully utilized through this assembly (LBL).

The ultimate purpose of using GQDs in PV cells is to use the sunlight optimally. GQDs in the active region of PV cells convert ultraviolet light into visible light, where the ultraviolet light is usually wasted due to zero deep penetration into the cells. This conversion ability of GQDs allows maximum use of sunlight absorption, where PV cell harnesses additional sunlight and contributes to high conversion efficiency [24]. Besides that, LBL assembly also leads to poor affinity of GQDs on to TiO_2 surface, which would reduce the amount of electron injected into the CB of TiO_2 with low charge collection efficiency [18]. On the other hand, if the morphological configuration of GQDs as co-sensitizer in DSSC changes from LBL into mixed form (GQDs+dye), GQDs can be utilized wholly. The mixed form allows GQDs to follow the type-II alignment and, at the same time to harness the additional solar light (acting as light absorbers). Since quantum dots may excite multiple photons simultaneously, a significant number of electrons can be injected into the metal oxide. Therefore, this work presents a novel morphological configuration to provide efficient charge transfer and potential for higher power conversion efficiency (PCE) for DSSC. Two types of assembly methods are studied in this work that are LBL and mixed.

2. Methodology

2.1 Materials and reagents

Oil palm empty fruit bunch fiber (OPEFB) mat was obtained from Malaysian Palm Oil Board, Malaysia. The chemical reagents, hydrogen peroxide (H_2O_2) (30% (w/w) in H_2O), sodium hydroxide (NaOH) (>> 98%), poly(ethylene glycol) (PEG) (average M_n 400), and N719 dye, were purchased from Sigma-Aldrich (USA). Fluorine-tin oxide (FTO), titania paste (Ti-nanoxide D/S, electrolyte (Iodolyte HI-30), and platinum paste (Platisol T/SP) were obtained from Solaronix.

2.2 Preparation of cellulose

Cellulose was produced from the OPEFB. The OPEFB fiber mat was cut and immersed in deionized water for 3 hours. After drying for two days under room temperature, the OPEFB was treated with 15% NaOH at 5:100 (m/mL) fiber to solution ratio. The sample was cooled to room temperature and rinsed with deionized water several times, followed by a bleaching process using H_2O_2 (10%) at 90°C-100°C for 1 h. The extracted cellulose was then dried in an oven at 60°C for 1 h.

2.3 Preparation of GQDs solution

GQDs were synthesized via a one-pot hydrothermal method. 20 mg of cellulose was added in 25 mL of deionized water. The suspension was then added with 0.2 g of PEG and homogenized with an ultrasonicator for 15 min. The suspension was subjected to a hydrothermal process in a 100 mL Teflon-lined stainless-steel autoclave placed into a convection oven at 200°C for 24 h. It was then naturally cooled to room temperature, and the product of brown liquid was centrifuged at 12000 rpm for 15 min to produce GQDs solution.

2.4 Preparation of photoanodes and QDSSCs

The TiO_2 photoanodes were prepared by the doctor blade technique. Two different methods were used to deposit GQDs solution onto the TiO_2 photoanodes: LBL and mixture methods. For the LBL method, the TiO_2 photoanodes were immersed in GQDs solution for 24 h and followed by N719 dye immersion on the next day for another 24 h. On the other hand, the mixture method involves mixing of 10 mL of GQDs solution and 5 mL of N719 solution (0.5 mM). The mixture was then stirred for 30 min on a hot plate using a magnetic stirrer. Then, the TiO_2 photoanodes were immersed with the GQDs+N719 mixture for 24 h at 60 °C. After the immersion process, the films were washed with ethanol to remove the excess dye. The QDSSC was assembled by dropping electrolyte into the space between the sensitized photoanode and platinum counter electrode, followed by sandwiching via binder clips. The morphological configurations using LBL and mixture assembly of QDSSC are illustrated in Figure 2.

2.5 Materials and device characterization

The structural properties of GQDs were analyzed via a high-resolution transmission electron microscope (HRTEM) (JEOL JEM-2100F, 200 kV). Raman spectra were analyzed by a confocal Raman Microscopy (Technospex uRaman-Ci; Nikon Eclipse Ci L laser microscope). Optical characterization of GQDs and the photoanodes were analyzed using UV-vis spectroscopy (Perkin Elmer Lambda 35) and photoluminescence spectrometer (Perkin Elmer Lambda 35). Chemical characterization was analyzed using an x-ray photoelectron spectrometer (XPS) (Kratos/Shimadzu; Axis Ultra DLD) and Fourier transform infrared (FTIR) (Agilent Technologies; Cary 630). Atomic force microscopy (AFM) (Park Systems; NX 10) under the mode of current sensing-atomic force microscopy (CS-AFM) and scanning kelvin probe microscopy (SKPM) analysis was done to investigate the local electrical potential between the mixture and LBL methods. The current density-voltage (J-V) characteristics (AutoLab) of the QDSSC were measured under a low illumination level of 0.5 mW/cm^2 using indoor lighting (halogen lamp). On the other hand, current density-voltage (J-V) characteristics under standard illumination level of 100 mW/cm^2 was measured using AAA class solar simulator (SSPN-X150T; Light Doctor Optical

Corporation, Taiwan) with IVDN-250E source meter. From this measurement, PV performance parameters such as fill-factor (FF), short-circuit current density (J_{sc}), open-circuit voltage (V_{oc}) and power conversion efficiency (η) were obtained. The electrochemical impedance spectroscopy (EIS) analysis was conducted using SMU-236 Keithly and Bard & Faulkner 2001) to study the electron transport in the QDSSC.

3. Results and discussion

3.1 Characterization of GQDs

Figure 3 shows the structural image of the synthesized GQDs. The thickness derived from AFM is 2.355 ± 0.86 nm corresponding to an average layer number of up to 5. The average lateral size determined by HRTEM is 9.87 ± 0.6 nm. The honeycomb hexagonal carbon network observed in the SAED pattern indicates that the GQDs are a single crystalline structure with fewer defects. It was later confirmed by the lattice (d) spacing of 0.2177 nm corresponding to graphene (100) planes. Figure 4 shows XPS and Raman analyzing the elemental compositions and functional groups. The high-resolution spectrum of C1s (Figure 4 (a)) is deconvoluted into three surface components, corresponding to C=C/C-C (284.8 eV), C-O (286.25 eV), and C=O (288.25 eV). The high-resolution spectrum of O1s (Figure 4 (b)) confirmed the presence of C=O (528.75 eV), C-OH (529.8 eV), and O=C-OH (533.25 eV) bonds. The O 1s spectrum reveals hydroxyl (-OH) functional group in the produced GQD. Furthermore, the GQDs have five pronounced excitonic absorption bands centered at about 207, 225, 241, and 258 nm as seen in Figure 4 (c). The peak at 258 nm was assigned to π-π* transition of C-O and aromatic C=C bonds in sp^2 hybridization [23]. The common weak shoulder at 400 nm observed for GQDs was not present in the synthesized GQDs, indicating no sp^3 defects within the graphene plane [23, 38]. The Raman spectrum of GQDs in Figure 4 (d) shows two prominent peaks around 1464 cm^{-1} (D-band) and 1527 cm^{-1} (G-band). The I_D/I_G intensity ratio is around 1.08 suggesting fewer structural defects in the graphene structure [29].

3.2 Characterization of the morphological configuration

3.2.1 Raman analysis

The Raman spectra of the TiO_2 and TiO_2 immersed in N719 dyes and GQDs solution is shown in Figure 5 (a). There are four major peaks (green region) observed at 143, 394, 513, 637 $cm^{-1,}$ which correspond to the E_g, B_{1g}, A_{1g}, and E_g phonon modes of anatase TiO_2 [39, 40]. Meanwhile, the peaks in the red region correspond to the N719 dye molecules. TiO_2-LBL and TiO_2-mixture samples with the addition of GQDs show a lower Raman intensity, which indicates a decrease in fluorescence signals. Figure 5 (b) is given by enlarging the red region (excluding the TiO_2 spectrum). The peaks ranging from 900 to 1800 cm^{-1} correspond to the C=C and C=N stretching bands of the bipyridine ring in the N719 dyes molecule structure. The small peak around 2100 cm^{-1} which represents the vibrations of C=N in the thiocyanate (SCN) groups [41]. With the addition of GQDs, the Raman signals for N719 dyes experienced a fluorescence quenching by electron transfer to the surface of GQDs [42]. Furthermore, the TiO_2-mixture sample exhibits lower

intensity than that of TiO_2-LBL due to a better π-π interaction between the GQDs and N719 molecules, further enhancing the fluorescence quenching effect. This can also further explain the peak shifting observed in the UV-Vis analysis (Figure 7a).

3.2.2 FTIR analysis

Figure 6 shows the FTIR spectra of TiO_2, TiO_2-N719, TiO_2-mixture, and TiO_2-LBL. The peaks at 3744 and 3367 cm^{-1} correspond to Ti-OH bonding, which exist in the surface of TiO_2 [40, 43]. A small peak around 1643 cm^{-1} indicates water molecules' presence on the TiO_2 surface [43]. Furthermore, the TiO_2-N719 sample shows peaks at around 1955, 1723, and 1530 $cm^{-1,}$ which correspond to thiocyanate (NCS), carbonyl (C=O), and C=C double bond [44], respectively. The spectra indicate the presence of N719 dye molecules adsorbed on the surface of TiO_2. Interestingly, the peaks which represent the N719 dye molecules were less dominant in TiO_2-mixture and TiO_2-LBL sample due to the interaction between GQDs and N719 dye molecules, causing the N719 to become less polar/dipole moment and also less IR sensitive. The shifting of the peak towards the lower wavenumber (3367 cm^{-1}) for the TiO_2-mixture sample is due to the lesser hydroxyl groups present on the surface of TiO_2, which allows a better surface intact of GQDs and N719 dye molecules on the TiO_2 surface.

3.2.3 UV-vis analyses

Figure 7 shows the absorption spectra of GQD, N719, and the mixture solution. The optical band gap (E_g) was determined by extrapolating the linear portion to the respective photon energy. The E_g of GQD and N719 was calculated to be 4.8 and 3.8 eV, respectively.

The peak deconvolution of the mixture sample (Figure 7b) is explained in detail in Figure 8. The peak at 230 nm corresponds to the C=C bonds of π to π* interaction and 300 nm attributes to the OH-C=O bonds of n to π* interaction. Meanwhile, 375 and 515 nm correspond to metal-ligand charge transfer of bipyridine ring and Ru^{2+}", respectively. Interestingly, the peak at around 230 nm shows a peak shifting to 245 nm for mixture, indicating π-π interaction between N719 and GQDs. Figure 8 (a) illustrates the interaction among TiO_2, N719 molecules, and triiodide molecules when it adsorbs light. The interaction between TiO_2 and N719 molecules is due to the bidentate κ^2 mode interaction between the carboxylic group on the bipyridine group of N719 molecule and the TiO_2 surface [44]. When the dye molecules adsorb photons, the aromatic bipyridine group excites its π electron to higher molecular orbitals excitation states. Then, the electron can be transferred to the TiO_2 via bidentate interaction of the carboxylic group. At this point, the N719 molecule will be in an unfavorable electronic state as the molecules have lost electrons. Next, the triiodide molecules will interact with the sulfur atom in the isocyanate group in the N719 molecule and transfers the electron into the N719 molecule to balance the electronic transition state of the molecule. In contrast, the triiodide will dissociate into I_2^- and I^- molecules [45, 46]. At the cathode part, its surface is coated with Pt will act as a catalytic surface for redox reaction to reduce the I^- molecules back to triiodide molecules [47].

Figure 8 (b) illustrates the π-π interaction between the GQDs and bipyridine group of the N719 molecule. The π-stacking of the molecules can induce the free nonbonding π electron to experience electron transfer between two molecules when excitation of electron occurs. When photon excites

the N719 molecules, the electron cloud of the N719 will be highly dense with free electrons that overlaps with the π molecular orbital of GQDs. Consequently, electrons are shared/transferred between these two molecules, which can avoid electron recombination and enhance the transfer of electrons into TiO_2 photoanode. Thus, this phenomenon explains the improvement of electron transfer and charge separation, which further supports the QDSSC device test's type-II alignment.

3.2.4 AFM analysis

The CS-AFM results figure out the current flow on the surface, as shown in Figure 9. An average current value of 1.284 pA was obtained for the GQDs sample measured at 2V, indicating the presence of GQDs on the surface. As for the mixture sample, the average current value dropped to 0.263 pA is due to the presence of N719 molecules, which disturbs the current flow between the surface and the cantilever probe.

The SKPM results explain the surface potential of the samples, as shown in Figure 10. The overall surface potential of N719 samples was 4.89 mV. When the sample was premixed with GQDs and N719, the overall surface potential increased by ~ 8 folds (33.47 mV). This phenomenon later explains the high Voc value in the QDSSC device measurement due to the compatible interaction between N719 molecules and GQDs, enhancing the electron mobility towards the photoanode [48].

3.2.5 Photoluminescence analysis

Figure 11 shows that when the excitation wavelength changed from 300 to 360 nm the emission peaks shift to the right from 419 to 434 nm. This range of peak emissions are due to the blue fluorescence of the GQD. The emission has a constant bathochromic shift of 50 nm with a rapidly decreasing intensity when the excitation extends to longer wavelengths. This phenomenon follows Stoke's-shift (PL emission of GQD has greater wavelength than the light used to excite the GQD), which can improve light absorption in the photoanode, providing larger J_{sc} in QDSSC [23]. Interestingly, the PL of the GQDs emits an extra peak at 361, 386, and 413 nm for each excitation at 320, 340, and 360 nm, respectively. These peaks correspond to the -OH groups of water molecules as water is the only solvent used for the synthesis of GQD.

Moreover, Figure 11 (a) shows the PL emission for TiO_2, TiO_2-N719, TiO_2-LBL and TiO_2-Mixture to test the energy transfer between the GQD and the N719 in different morphological configurations. TiO_2-LBL and TiO_2-Mixture samples exhibit the same quenching rate at 419 nm (UV-region). However, TiO_2-Mixture shows the highest PL quenching at the visible range, indicating a higher percentage of excited electrons have been injected into the CB of TiO_2. Compared with the TiO_2-N719 sample, the addition of GQDs provides higher PL quenching than that of without GQDs. The result reveals that mixture configuration gives efficient electron injection which assists in the high PCE of the solar cell. Furthermore, the overlapping of TiO_2-N719 absorbance and PL of GQD realizes the possibility of Forster resonance energy transfer (FRET) type charge transfer as observed in Figure 11 (c). The more considerable degree of overlap between the donor PL spectrum and the acceptor absorbance spectrum belonging to TiO_2-Mixture

indicates that a more generous amount of light can be utilized by N719 via the function of GQD as donor and FRET [25].

3.2.6 Photovoltaic Performance

The PV performance was investigated under two conditions: indoor lighting (low light illumination level) and sunlight (standard illumination level). Figure 12 shows the J-V curves measured under 0.5 mW/cm^2 for the three TiO_2-DSSCs using N719, mixture of GQDs+N719 and LBL of GQDs/N719 as photosensitizers. Subsequently, Table 1 lists the PV parameters obtained from the J-V curves.

The TiO_2-DSSC sensitized using the LBL method of GQD/N719 showed an improved PCE of 32.54% (= 16.76%) with respect to the TiO_2-DSSC sensitized by a mixture of GQD+N719 (= 12.07%). Both are much higher than the TiO_2-DSSC sensitized with a common dye of N719 (= 9.58%). The V_{oc} values remain at 0.70 V for all cells. Figure 12 shows that the J_{sc} and V_{oc} characteristics of GQD mixture and LBL method were higher than the TiO_2-DSSC sensitized with N719. Moreover, the incorporation of GQD has sharply increased the FF value for the mixture method of GQD+N719, but the J_{sc} dropped to 0.186 mA/cm^2. This is due to the very low light intensity of 0.5 mW/cm^2 that affects the amount of photogenerated electron flow through the cell. This phenomenon also flattens V_{oc} at 0.70 V and increases FF. Since V_{oc} is defined as the difference between the Fermi level of TiO_2 and redox potential of the electrolyte, V_{oc} is diminished with the decrease in the amount of electrons in the TiO_2 photoanode layer [49]. In contrast, it reported that DSSCs are less affected by light intensity [50]. Whereby under low light illumination, less oxidized dyes are generated, and those oxidized dyes are rapidly regenerated by the iodide ions (I^-) in the electrolyte and hence, less tri-iodide ions (I_3^-) are regenerated at the surface of the counter electrode. Later, DSSC can provide sufficient charges for reducing tri-iodide ions but with less amount of electron. This event would then influence the decrease of J_{sc}.

Figure 13 and Table 2 present the J-V curves and PV parameters obtained from the three TiO_2-DSSCs illuminated under 100 mW/cm^2 xenon lamp, respectively. A comparison between low and standard illumination upon the cells includes increased V_{oc} values from 0.70 V to 0.75 V (maximum value for GQD+N719 sample), indicating reduces in back electron transfer. The TiO_2-DSSC with the mixture of GQD+N719 also exhibited the highest J_{sc} of 5.075 mA/cm^2 and of 2.906%. The same phenomenon occurs in the LBL sample, whereby the J_{sc} and increase up to 34% and 28.73%, respectively, compared to the cell sensitized with the N719 dye. Kumar et al. reported that GQD has a similar role as the dye, which can generate electrons by a single photon [51]. This ability will infuse more electrons into the TiO_2 photoelectrode and, therefore, improve J_{sc} and of the DSSCs. Moreover, Mustafa and Sulaiman stated that TiO_2 decorated with GQD performs as a light scattering layer (LSL) and, therefore, increases the optical path length and increases incident light [52]. Hence, the LSL trapped extra light, excites more dye molecules, produces more electron (photocurrent), and increases the power conversion efficiency of the DSSC.

In general, when DSSC is under illumination, the dye molecules absorb the light (photon) and excites electrons into the lowest unoccupied molecular orbital (LUMO) energy level before

transfers to the CB of TiO_2's photoanode. Then, the electron moves to the transparent conductive substrate of the photoanode, travel through the external circuit, and is collected on the surface of the Pt counter electrode, while the redox system simultaneously regenerates the oxidized dye in the electrolyte solution of I^-/I_3^- [53, 54]. Figure 14 shows the respective electron mechanism in TiO_2-DSSC sensitized with GQD and N719. It is clearly seen that this mechanism follows the type-II energy level. The position of CB for TiO_2 is 4.45 eV versus the absolute vacuum scale, and the LUMO state of GQD is higher than the CB of TiO_2. When the TiO_2-DSSC is illuminated by visible light, the dye molecules absorb the light, and photogenerated electrons of GQD are aptly excited from LUMO energy level into CB of TiO_2.

Moreover, a mismatch between the LUMO states of the GQD and N719 induces a step-like energy band structure, which aids the electron from the N719 dye LUMO level descend to the TiO_2 photoelectrode through the GQD LUMO level. This mechanism not just improve the electron injection but also gain higher efficiency. The role of GQD as a charge separator is also observed in Figure 14. The GQD between the TiO2 and N719 restricts the injected electron to recombine back with the redox electrolyte and restricts the electron-hole recombination in the HOMO of N719. Hence, the electron transfers from LUMO of GQD to TiO_2 CB is thermodynamically promising [55].

The results demonstrated that by introducing the GQD, the performance of the photoelectrode under low and standard illumination has significantly improved. Salam et al. reported the high efficiency of the DSSCs is due to the following factors [56]:

1. highly porous nature of TiO_2 nanoparticles with the addition of GQDs allows more N719 dye molecules to get adsorbed, leading to a generation of a more significant number of photoelectrons and hence increase the value of J_{sc},
2. faster transport of photogenerated electrons from N719 dye to CB of TiO_2 due to presence of GQD onto the TiO_2 as shown by TEM analysis,
3. reduction in back carrier recombination's due to the highly conductive nature of GQD onto the TiO_2 photoelectrode layer, which does not allow the photogenerated electrons to go into a deep state.

Generally, the above factors contribute to the increased in the J_{sc} and FF of the DSSCs. Recently, Jahantigh et al. reported that the presence of amino functional groups on the GQD surface also attracted TiO_2 nanocomposite surface structure and therefore leads to better charge injection and improved the DSSCs [55].

3.2.7 EIS Analysis

The EIS analysis was conducted to investigate the electron transport properties inside the mesoporous TiO_2 photoanode film, electron recombination event at the TiO_2/electrolyte interface, charge transfer at the counter electrode and diffusion of redox couple in the electrolyte based upon the impedance response over frequency. The respective impedance spectra or Nyquist plots for TiO_2-DSSCs sensitized with N719, a mixture of GQD+N719, and layer by layer of GQD/N719 are shown in Figure 15, and their corresponding impedance parameters are listed in Table 3. A standard Nyquist plot comprises of three semicircles. The first semicircle at the high-frequency

region represents a parallel combination of the counter electrode charge transfer resistance (R_{Pt}) and Helmholtz capacitance (C_{Pt}) at the platinum counter electrode/electrolyte interface. The largest semicircles at medium frequency correspond to charge transfer resistance of the charge recombination process at TiO_2+GQD+N719/electrolyte interface (R_{ct}) and chemical capacitance (C_{dl}) of the TiO_2 film (photoanode electrode). The third semicircle at the low-frequency region resembles the finite Warburg impedance due to the diffusion process of iodide/tri-iodide ions in the electrolyte (Z_d) [57-61]. However, the undefined semicircle shape that represents Z_d cannot be seen in the obtained plot. Moreover, a simple equivalent circuit model (as shown in Figure 15 (c)) representing the DSSC is used to fit the Nyquist plot and obtain the electron transport parameters at different open-circuit voltage frequencies.

Hence, charge collection efficiency (η_c) can be extracted from the EIS analysis using the following equation (1) [52],

$$\eta_c = \left(1 + \frac{R_s}{R_{ct}}\right)^{-1} \tag{1}$$

where R_s represents series resistance, including the sheet resistance of the TCO glass and the contact resistance of the cell. From the results in Table 3, TiO_2-DSSC with GQD+N719 exhibits higher charge collection efficiency (η_c) of 0.96 compared to the LBL sample of QGD/N719 (η_c = 0.94). Although the difference between the two values is meager (2.11%), it demonstrated a better light absorption effect than the latter. The results are also matching with higher J_{sc} values measured from the PV performance. Recently, Ali et al. reported an improvement in PCE of mixed GQD+N719 is due to rapid electron transport, enhanced electron collection at the TiO_2 photoanode, and improved light-harvesting efficiency of the cell [48]. Since the LUMO level of GQD is higher than CB of TiO_2, the thermodynamics effect aids the electron transfer mechanism. Under illumination effect, more electron transfer occurs from the LUMO level state of GQD to the CB of TiO_2 [62].

Moreover, the Bode plot analysis can be extracted from EIS analysis to analyze the samples' effective electron lifetime (τeff). The values of τ_{eff} can be obtained from the maximum peak frequency (f_{max}) of the spectra that represents the photoanode in the medium frequency region. This maximum frequency also represents the effective rate constant for recombination with tri-iodide ions (k_{eff}). These parameters can be correlated as in equations (2) and (3),

$$\tau_{eff} = \frac{1}{\omega_{ct}} = \frac{1}{2\pi f_{max}} \tag{2}$$

$$\omega_{max} = k_{eff} = \frac{1}{\tau_{eff}} \tag{3}$$

where ω_{ct} is an angular frequency of electron recombination reaction and ω_{max} is the maximum angular frequency at the state of electron recombination reaction with tri-iodide ions [57-59, 63].

As highlighted in Table 3, the mixture of GQD+N719 exhibit longer electron lifetime, τ_{eff} of 1.293 ms compared to the TiO_2 layered with GQD/N719 (τ_{eff} =1.264 ms). Whereby it indicates a suppress recombination event and therefore leads to higher efficiency. In contrast, Mustafa and Sulaiman reported bigger R_{ct} will hinder the electron flow to complete the electron-regeneration process and increase internal resistance [52]. This phenomenon indicates that the incorporation of the GQD+N719 mixture increases the overall resistance of the TiO_2-DSSC photoanode.

Conclusion

In summary, GQDs produced from a waste material of OPEFB without utilizing harsh acids were successfully employed in QDSSC. Interestingly, the LBL method exhibited the highest efficiency of 16.76 % under low illumination but a lower efficiency than the mixture method under standard light illumination. The high solar power conversion efficiency obtained by the mixture-QDSSC is mainly due to the π-π interaction between the GQDs and N719 molecules with a red-peak shift in UV-Vis, which further enhances the fluorescence quenching effect in Raman. Mixture-FTIR also reveals that fewer -OH groups were present on the surface of TiO_2, which allows a better surface intact of GQDs and N719 dye molecules on the TiO_2 surface, promoting good affinity between GQDs and TiO_2. The significant increment of J_{sc} for the mixture sample under standard light illumination is an indication that the scattered N719 and GQDs molecules on top of TiO_2 maximized the light absorption covering from UV until the visible region. Accordingly, the mixture sample obtained high charge collection efficiency demonstrating enhanced electron collection at the TiO_2 photoanodes, better light-harvesting efficiency, and longer electron lifetime. The highest PL quenching at the visible region for the mixture sample exhibited a large amount of photogenerated electrons in the CB of TiO_2. Additionally, V_{oc} was also improved from 0.7 (LBL) to 0.75 V (mixture), indicating a reduction in back electron transfer due to the highly conductive nature of GQDs onto the TiO2 photoelectrode layer does not allow the photogenerated electrons to go into deep state. This was evident when the sample was premixed with GQDs and N719; the overall surface potential increased by ~ 8 folds (33.47 mV). This conclusion is supported by the result obtained for mixture-QDSSC with the highest efficiency. The GQDs realized a cascaded type-II alignment of the energy level, and N719 dye absorbs light over the visible spectrum. This type-II system fulfills the primer conditions of: (i) greater overlap between the mixture absorbance and GQDs emission spectra, and (ii) larger gap of GQDs donor (4.83 eV) than the gap of dye acceptor (3.85 eV). Therefore, it is reasonable to conclude that the mixture morphological configuration of co-sensitization is an effective mediator for light-harvesting in QDSSC.

Author Contributions

All the authors have contributed to this research article such as: Conceptualization, S.Mahalingam and A.Manap; Data curation, S.Mahalingam, K.S.Lau, and A.Omar; Formal analysis, S.Mahalingam, K.S.Lau, A.Omar, and I.J.Mathews; Funding acquisition, A.Manap; Investigation, S.Mahalingam, K.S.Lau, A.Omar, I.J.Mathews; Methodology, S.Mahalingam, K.S.Lau, A.Omar, P. Chelvanathan, I.J.Mathews, A.Manap and NF.Afandi; Project administration, A.Manap;

Resources, N.Amin, C.H.Chia, P.Chelvanathan, and N.AbdRahim; Software, I.J.Mathews; Supervision, A.Manap; Validation, A.Manap; Writing – original draft, S.Mahalingam, K.S.Lau, and A.Omar; Writing–review and editing, A.Manap, P.Chelvanathan, C.H.Chia, and N.Amin.

Acknowledgment

The authors would like to thank the Ministry of Higher Education Malaysia (MoHE) and Universiti Tenaga Nasional (UNITEN) for funding this study under the Fundamental Research Grant Scheme (FRGS) of Grant No. FRGS/1/2019/STG07/UNITEN/02/3, BOLDREFRESH2025 of Grant No. J5100D4103, UNITEN BOLD of Grant No. RJO10517844/070, Telkom University-Uniten International Collaboration Grant of Grant No. 2020101TELCO, and Universitas Pertamina-Uniten International Collaboration Grant of Grant No. 2020001YCUPU.

Competing Interest

The author(s) declare no competing interests.

References

[1] O'regan B, Grätzel M. A low-cost, high-efficiency solar cell based on dye-sensitized colloidal TiO 2 films. nature. 1991 Oct;353(6346):737-40.

[2] Zardari P, Rostami A, Shekaari H. p-Phenylenediaminium iodide capping agent enabled self-healing perovskite solar cell. Scientific reports. 2020 Nov 17;10(1):1-4.

[3] Bagher, Askari Mohammad; Mirzaei , Mahmoud Abadi Vahid; Mirhabibi Mohsen, "Types of Solar Cells and Application," *American Journal of Optics and Photonics,* vol. 3, no. 5, pp. 94-113, 2015.

[4] Kumar KA, Pandurangan A, Arumugam S, Sathiskumar M. Effect of bi-functional hierarchical flower-like CoS nanostructure on its interfacial charge transport kinetics, magnetic and electrochemical behaviors for supercapacitor and DSSC applications. Scientific reports. 2019 Feb 4;9(1):1-6.

[5] Ramarajan R, Purushothamreddy N, Dileep RK, Kovendhan M, Veerappan G, Thangaraju K, Joseph DP. Large-area spray deposited Ta-doped SnO2 thin film electrode for DSSC application. Solar Energy. 2020 Nov 15;211:547-59.

[6] Mahalingam S, Abdullah H. Electron transport study of indium oxide as photoanode in DSSCs: A review. Renewable and Sustainable Energy Reviews. 2016 Sep 1;63:245-55.

[7] Mahalingam S, Abdullah H, Manap A. Role of acid-treated CNTs in chemical and electrochemical impedance study of dye-sensitised solar cell. Electrochimica Acta. 2018 Feb 20;264:275-83.

[8] G. C. Deyang Li, "Upconversion-Enhanced Dye-Sensitized Solar Cells," *Dye-Sensitized Solar Cells,* pp. 325-340.

[9] Zhou C, Jiang W, Via BK. Facile synthesis of soluble graphene quantum dots and its improved property in detecting heavy metal ions. Colloids and Surfaces B: Biointerfaces. 2014 Jun 1;118:72-6.

[10] Ahmadi H, Keshipour S, Ahour F. New water-soluble colorimetric pH and metal ione sensor based on graphene quantum dot modified with alizarine red S. Scientific Reports. 2020 Aug 25;10(1):1-9.

[11] Huang D, Zhou H, Wu Y, Wang T, Sun L, Gao P, Sun Y, Huang H, Zhou G, Hu J. Bottom-up synthesis and structural design strategy for graphene quantum dots with tunable emission to the near infrared region. Carbon. 2019 Feb 1;142:673-84.

[12] Umrao S, Jang MH, Oh JH, Kim G, Sahoo S, Cho YH, Srivastva A, Oh IK. Microwave bottom-up route for size-tunable and switchable photoluminescent graphene quantum dots using acetylacetone: New platform for enzyme-free detection of hydrogen peroxide. Carbon. 2015 Jan 1;81:514-24.

[13] Xie JD, Lai GW, Huq MM. Hydrothermal route to graphene quantum dots: Effects of precursor and temperature. Diamond and Related Materials. 2017 Oct 1;79:112-8.

[14] Shin Y, Park J, Hyun D, Yang J, Lee JH, Kim JH, Lee H. Acid-free and oxone oxidant-assisted solvothermal synthesis of graphene quantum dots using various natural carbon materials as resources. Nanoscale. 2015;7(13):5633-7.

[15] Pan D, Zhang J, Li Z, Wu M. Hydrothermal route for cutting graphene sheets into blue-luminescent graphene quantum dots. Advanced materials. 2010 Feb 9;22(6):734-8.

[16] Chen W, Shen J, Lv G, Li D, Hu Y, Zhou C, Liu X, Dai Z. Green synthesis of graphene quantum dots from cotton cellulose. ChemistrySelect. 2019 Mar 14;4(10):2898-902.

[17] Y. H. Y. Z. G. S. L. D. Y. H. L. Q. Yan Li, "An Electrochemical Avenue to Green-Luminescent Graphene Quantum Dots as Potential Electron-Acceptors for Photovoltaics," *Advanced Materials,* vol. 23, no. 6, pp. 776-780, 2010.

[18] X. C. B. L. L.-s. L. Xin Yan, "Large, Solution-Processable Graphene Quantum Dots as Light Absorbers for Photovoltaics," *Nano Letters,* vol. 10, no. 5, pp. 1869-1873, 2010.

[19] Kim J, Lee B, Kim YJ, Hwang SW. Enhancement of dye-sensitized solar cells efficiency using graphene quantum dots as photoanode. Bull Korean Chem Soc 2019;40:56–61.

[20] Zamiri G, Bagheri S. Fabrication of green dye-sensitized solar cell based on ZnO nanoparticles as a photoanode and graphene quantum dots as a photo-sensitizer. J Colloid Interface Sci 2018;511:318–24.

[21] Dutta M, Sarkar S, Ghosh T, Basak D. ZnO/graphene quantum dot solid-state solar cell. J Phys Chem C 2012;116:20127–31.

[22] M Sharif NF, Kadir MZAA, Shafie S, Rashid SA, Wan Hasan WZ, Shaban S. Charge transport and electron recombination suppression in dye-sensitized solar cells using

graphene quantum dots. Results Phys 2019;13:102171.

[23] Mihalache I, Radoi A, Mihaila M, Munteanu C, Marin A, Danila M, et al. Charge and energy transfer interplay in hybrid sensitized solar cells mediated by graphene quantum dots. Electrochim Acta 2015;153:306–15.

[24] Kundu S, Sarojinijeeva P, Karthick R, Anantharaj G, Saritha G, Bera R, et al. Enhancing the Efficiency of DSSCs by the Modification of TiO_2 Photoanodes using N, F and S, co-doped Graphene Quantum Dots. Electrochim Acta 2017;242:337–43.

[25] Lee E, Ryu J, Jang J. Fabrication of graphene quantum dots via size-selective precipitation and their application in upconversion-based DSSCs. Chem Commun 2013;49:9995.

[26] Fang X, Li M, Guo K, Li J, Pan M, Bai L, et al. Graphene quantum dots optimization of dye-sensitized solar cells. Electrochim Acta 2014;137:634–8.

[27] Majumder T, Dhar S, Chakraborty P, Debnath K, Mondal SP. Advantages of ZnO nanotaper photoanodes in photoelectrochemical cells and graphene quantum dot sensitized solar cell applications. J Electroanal Chem 2018;813:92–101.

[28] Majumder T, Debnath K, Dhar S, Hmar JJL, Mondal SP. Nitrogen-doped graphene quantum dot-decorated zno nanorods for improved electrochemical solar energy conversion. Energy Technol 2016;4:950–8.

[29] Kolay A, Kokal RK, Kalluri A, Macwan I, Patra PK, Ghosal P, et al. New antimony selenide/nickel oxide photocathode boosts the efficiency of graphene quantum-dot co-sensitized solar cells. ACS Appl Mater Interfaces 2017;9:34915–26.

[30] Porfarzollah A, Mohammad-Rezaei R, Bagheri M. Ionic liquid-functionalized graphene quantum dots as an efficient quasi-solid-state electrolyte for dye-sensitized solar cells. J Mater Sci Mater Electron 2020;31:2288–97.

[31] Chen L, Guo CX, Zhang Q, Lei Y, Xie J, Ee S, et al. Graphene quantum-dot-doped polypyrrole counter electrode for high-performance dye-sensitized solar cells. ACS Appl Mater Interfaces 2013;5:2047–52.

[32] Dinari M, Momeni MM, Goudarzirad M. Dye-sensitized solar cells based on nanocomposite of polyaniline/graphene quantum dots. J Mater Sci 2016;51:2964–71.

[33] Yu C, Liu Z, Chen Y, Meng X, Li M, Qiu J. CoS nanosheets-coupled graphene quantum dots architectures as a binder-free counter electrode for high-performance DSSCs. Sci China Mater 2016;59:104–11

[34] Lee CP, Lin CA, Wei TC, Tsai ML, Meng Y, Li CT, et al. Economical low-light photovoltaics by using the Pt-free dye-sensitized solar cell with graphene dot/PEDOT: PSS counter electrodes. Nano Energy 2015;18:109–17.

[35] Chang Q, Ma Z, Wang J, Li P, Yan Y, Shi W, et al. Hybrid graphene quantum dots@graphene foam nanosheets for dye-sensitized solar cell electrodes. Energy Technol 2016;4:256–62.

[36] Teymourinia H, Salavati-Niasari M, Amiri O, Farangi M. Facile synthesis of graphene quantum dots from corn powder and their application as down conversion effect in quantum

dot-dye-sensitized solar cell. J Mol Liq 2018;251:267–72.

[37] Mora-Seró I, Gross D, Mittereder T, Lutich AA, Susha AS, Dittrich T, et al. Nanoscale interaction between CdSe or CdTe nanocrystals and molecular dyes fostering or hindering directional charge separation. Small 2010;6:221–5.

[38] Wang L, Wang Y, Xu T, Liao H, Yao C, Liu Y, Li Z, Chen Z, Pan D, Sun L, Wu M. Gram-scale synthesis of single-crystalline graphene quantum dots with superior optical properties. Nature communications. 2014 Oct 28;5(1):1-9.

[39] Challagulla S, Tarafder K, Ganesan R, Roy S. Structure sensitive photocatalytic reduction of nitroarenes over TiO 2. Scientific reports. 2017 Aug 18;7(1):1-1.

[40] Singh R, Dutta S. Synthesis and characterization of solar photoactive TiO2 nanoparticles with enhanced structural and optical properties. Advanced Powder Technology. 2018 Feb 1;29(2):211-9.

[41] Wang X, Wang Y, Sui H, Zhang X, Su H, Cheng W, Han XX, Zhao B. Investigation of charge transfer in Ag/N719/TiO2 interface by surface-enhanced Raman spectroscopy. The Journal of Physical Chemistry C. 2016 Jun 23;120(24):13078-86.

[42] Kagan MR, McCreery RL. Reduction of fluorescence interference in Raman spectroscopy via analyte adsorption on graphitic carbon. Analytical chemistry. 1994 Dec 1;66(23):4159-65.

[43] Azami MS, Nawawi WI, Jawad AH, Ishak MA, Ismail K. N-doped TiO2 synthesised via microwave induced photocatalytic on RR4 dye removal under LED light irradiation. Sains Malays. 2017 Aug 1;46(8):1309-16.

[44] Singh J, Gusain A, Saxena V, Chauhan AK, Veerender P, Koiry SP, Jha P, Jain A, Aswal DK, Gupta SK. XPS, UV–vis, FTIR, and EXAFS studies to investigate the binding mechanism of N719 dye onto oxalic acid treated TiO2 and its implication on photovoltaic properties. The Journal of Physical Chemistry C. 2013 Oct 17;117(41):21096-104.

[45] Vaghasiya JV, Sonigara KK, Suresh L, Panahandeh-Fard M, Soni SS, Tan SC. Efficient power generating devices utilizing low intensity indoor lights via non-radiative energy transfer mechanism from organic ionic redox couples. Nano Energy. 2019 Jun 1;60:457-66.

[46] Boschloo G, Hagfeldt A. Characteristics of the iodide/triiodide redox mediator in dye-sensitized solar cells. Accounts of chemical research. 2009 Nov 17;42(11):1819-26.

[47] Zhang B, Wang D, Hou Y, Yang S, Yang XH, Zhong JH, Liu J, Wang HF, Hu P, Zhao HJ, Yang HG. Facet-dependent catalytic activity of platinum nanocrystals for triiodide reduction in dye-sensitized solar cells. Scientific reports. 2013 May 14;3:1836.

[48] Marchat C, Dai L, Alvarez J, Le Gall S, Kleider JP, Misra S, i Cabarrocas PR. Local V OC Measurements by Kelvin Probe Force Microscopy Applied on PIN Radial Junction Si Nanowires. Nanoscale Research Letters. 2019 Dec;14(1):1-8.

[49] [35] Chou, J.-C., Kuo, C.-H., Kuo, P.-Y., Lai, C.-H., Nien, Y.H., Liao, Y.-H., Ko, C.-C., Yang, C.-M., Wu, C.-Y., 2019. The retardation structure for improvement of photovoltaic performance of dye-sensitized solar cell under low illumination. IEEE J. Photovoltaics 9 (3), 926-933. https://doi.org/10.1109/JPHOTOV.2019.2896054

[50] Lee, C.-P., Lin, C.-A., Wei, T.-C., Tsai, M.-L., Meng, Y., Li, C.-T., Ho, K.-C., Wu, C.-I, Lau, S.-P., He, Jr.-H. 2015. Economical low-light photovoltaics by using the Pt-free dye-sensitized solar cell with graphene dot/PEDOT:PSS counter electrodes. Nano Energy 18, 109-117. http://dx.doi.org/10.1016/j.nanoen.2015.10.008

[51] Kumar, Y.R., Deshmukh, K., Sadasivuni, K.K., Pasha, S.K.K. 2020. Graphene quantum dot based materials for sensing, bio-imaging and energy storage applications: a review. RSC Adv., 10, 23861-23898. https://doi.org/10.1039/D0RA03938A

[52] Mustafa, M.N., Sulaiman, Y. 2020. Optimization of titanium dioxide decorated by graphene quantum dot as a light scatterer for enhanced dye-sensitized solar cell performance. J. Electroanalytical Chem. 876, 114516.

[53] Karim, N.A., Mehmood, U., Zahid, H.F., Asif, T., 2019. Nanostructured photoanode and counter electrode materials for efficient dye-sensitized solar cells (DSSCs). Sol. Energy 185, 165-188. https://doi.org/10.1016/j.solener.2019.04.057

[54] Fan, K., Yu, J., Ho, W., 2017. Improving photoanodes to obtain highly efficient dye-sensitized solar cells: A brief review. Mater. Horiz. 4 (3), 319-344. https://doi.org/10.1039/C6MH00511J

[55] Jahantigh, F., Ghorashi, S.M.B., Mozaffari, S. 2020. Orange photoluminescent N-doped graphene quantum dots as an effective co-sensitizer for dye-sensitized solar cells. J. Sol. State Electrochem. 24, 883-889. https://doi.org/10.1007/s10008-020-04515-3

[56] Salam, Z., Vijayakumar, E., Subramania, A., Sivasankar, N., Mallick, S., 2015. Graphene quantum dots decorated electrospun TiO2 nanofibers as an effective photoanode for dye sensitized solar cells. Sol. Energy Mater. Sol. Cells 143, 250-259. http://dx.doi.org/10.1016/j.solmat.2015.07.001

[57] [Adachi, M., Sakamoto, M., Jiu, J., Ogata, Y., Isoda, S., 2006. Determination of parameters of electron transport in dye-sensitized solar cells using electrochemical impedance spectroscopy. J. Phys. Chem. B 110 (28), 13872-13880. https://doi.org/10.1021/jp061693u

[58] Bisquert, J., 2002. Theory of the impedance of electron diffusion and recombination in a thin layer. J. Phys. Chem. B 106 (2), 325-333. https://doi.org/10.1021/jp011941g

[59] Omar, A., Abdullah, H., 2014. Electron transport analysis in zinc oxide-based dye-sensitized solar cells: A review. Renew. Sustain. Energy Rev. 31, 149-157. https://doi.org/10.1016/j.rser.2013.11.031

[60] Fabregat-Santiago, F., Bisquert, J., Garcia-Belmonte, G., Boschloo, G., Hagfeldt, A., 2005. Influence of electrolyte in transport and recombination in dye-sensitized solar cells studied by impedance spectroscopy. Sol. Energy Mater. Sol. Cells 87 (1), 117-131. https://doi.org/10.1016/j.solmat.2004.07.017

[61] Wang, Q., Moser, J.-E., Grätzel, M., 2005. Electrochemical impedance spectroscopic analysis of dye-sensitized solar cells. J. Phys. Chem. B 109 (31), 14945-14953. https://doi.org/10.1021/jp052768h

[62] Ali, H.H., Al-bahrani, M.R. 2020. Synthesis of TiO2/graphene quantum dots as photoanode to enhance power conversion efficiency for dye-sensitized solar cells. Inter. J. Adv. Sci.

Tech. 29 (3), 11071-11081.

[63] Omar, A., Abdullah, H., Yarmo, M.A., Shaari, S., Taha, M.R., 2013. Morphological and electron transport studies in ZnO dye-sensitized solar cells incorporating multi- and single-walled carbon nanotubes. J. Phys. D Appl. Phys. 46 (16), 165503. https://doi.org/10.1088/0022-3727/46/16/165503

Figure Legends

Fig. 1. Type-II alignment of GQD and dye in QDSSC

Fig. 2. Morphological configuration of (**a**) LBL and (**b**) mixture assembly in QDSSC

Fig. 3. (**a**) AFM image of GQDs height, HRTEM images of GQDs with (**b**) average diameter, (**c**) SAED pattern, and (**d**) lattice fringe

Fig. 4. GQDs XPS spectra of (**a**) C1s and (**b**) O1s, (**c**) absorbance of GQDs, and (**d**) Raman spectrum of GQDs

Fig. 5. Raman spectra of TiO_2, TiO_2-N719, TiO_2-mixture, and TiO_2-LBL with (**a**) full-spectrum and (**b**) zoomed-in image of red region from graph (a) excluding TiO_2 spectrum

Fig. 6. FTIR spectra of TiO_2, TiO_2-N719, TiO_2-mixture, and TiO_2-LBL

Fig. 7. Absorbance of (**a**) peak fitting of GQDs, N719 and mixture solution, (**b**) peak deconvolution of mixture solution and Tauc plots of (**c**) GQD and (d) N719

Fig. 8. Illustration of (**a**) interaction among TiO_2, N719, and triiodide molecules, and (**b**) π-π interaction between GQDs and bipyridine group of N719

Fig. 9. AFM topography of (**a**) GQDs and (**c**) mixture, and CS-AFM measurement of (**b**) GQDs and (**d**) mixture

Fig. 10. AFM topography of (**a**) N719 and (**c**) mixture, and SKPM measurement of (**b**) N719 and (**d**) mixture

Fig. 11. Photoluminescence of (**a**) GQDs, and (**b**) thin film samples and (**c**) absorbance of TiO_2-mixture and TiO_2-N719 and photoluminescence of GQDs to support FRET mechanism

Fig. 12. J-V curves measured under 0.5 mW/cm^2 of low illumination for TiO_2-DSSC sensitized with N719, mixture, and LBL

Fig. 13. J-V curves under 100 mW/cm^2 illumination for TiO_2-DSSC sensitized with N719, mixture, and LBL

Fig.14. Energy band structure and electron mechanism in the TiO_2-DSSC sensitized with GQD, and N719

Fig. 15 (**a**) A simple equivalent circuit, (**b**) fitted Nyquist plot and (**c**) Bode plot of TiO_2-DSSC sensitized with N719, mixture, and LBL

Figures

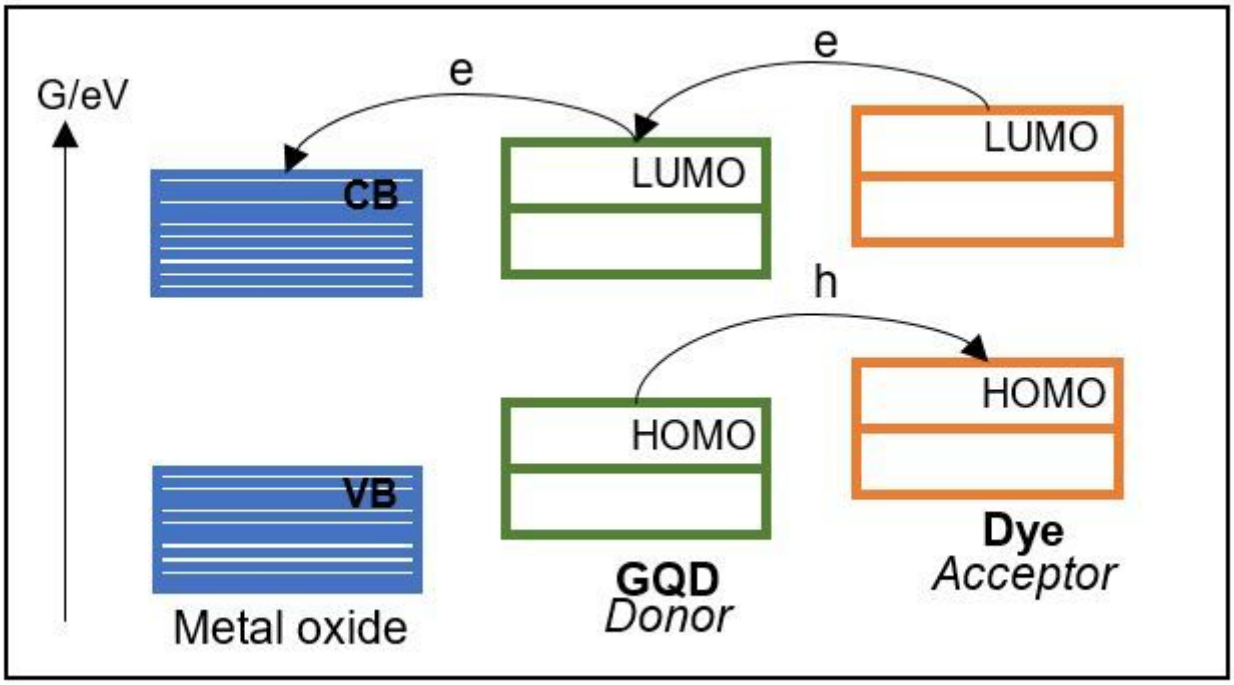

Figure 1

Type-II alignment of GQD and dye in QDSSC

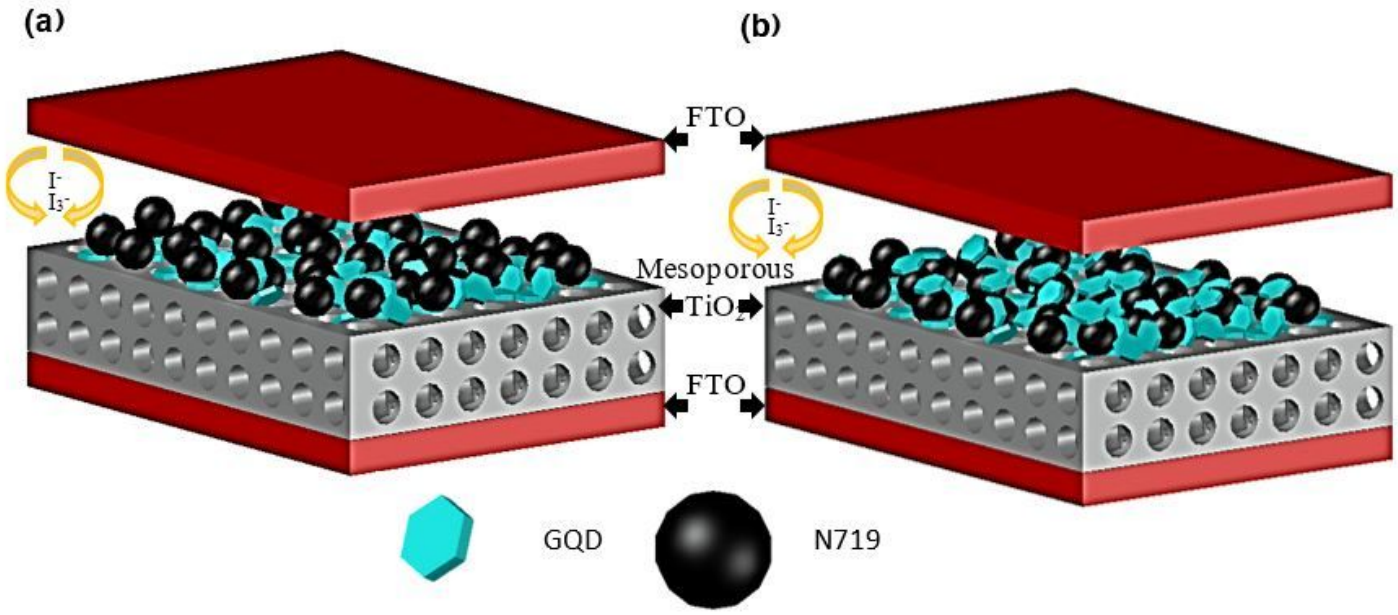

Figure 2

Morphological configuration of (a) LBL and (b) mixture assembly in QDSSC

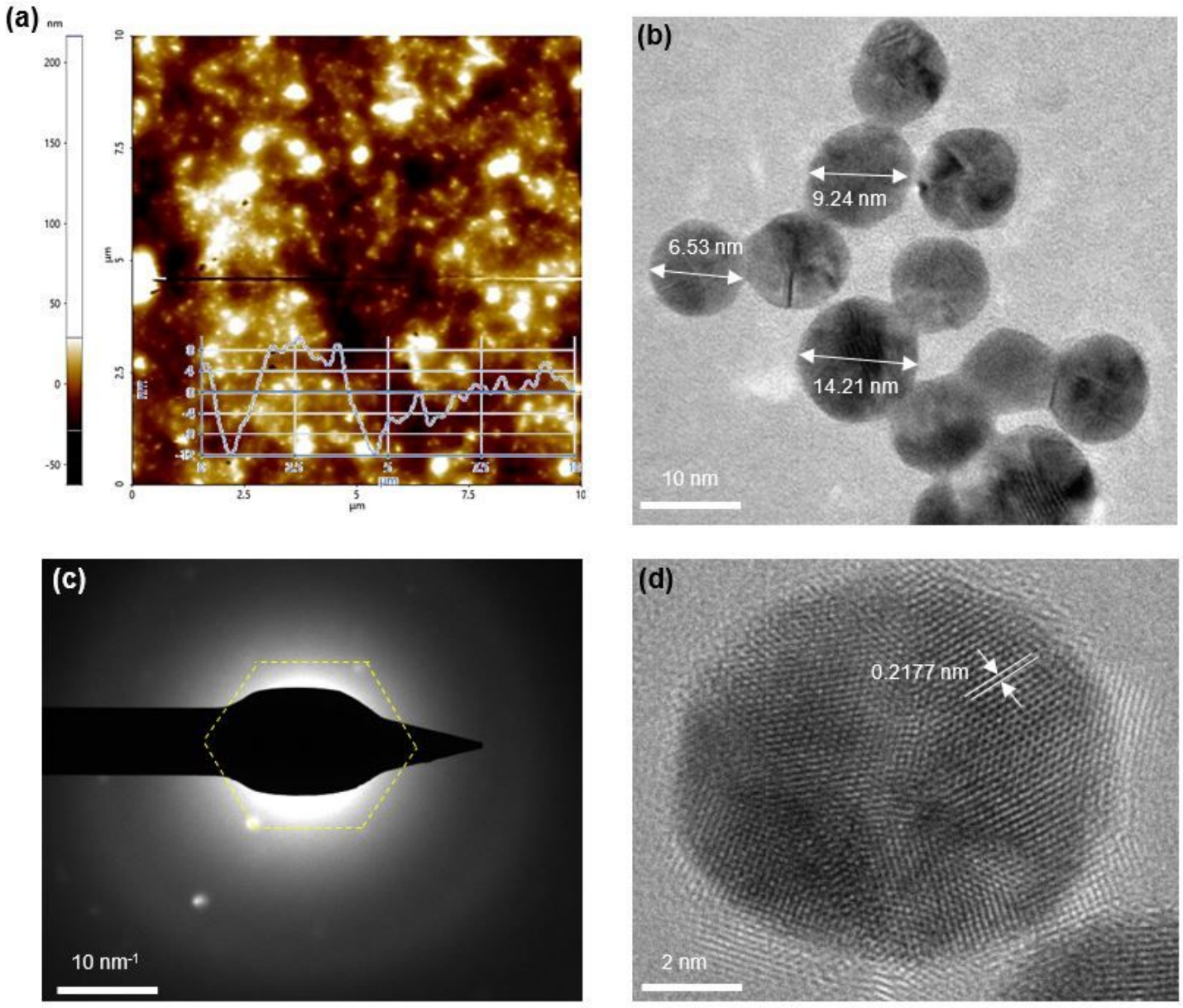

Figure 3

(a) AFM image of GQDs height, HRTEM images of GQDs with (b) average diameter, (c) SAED pattern, and (d) lattice fringe

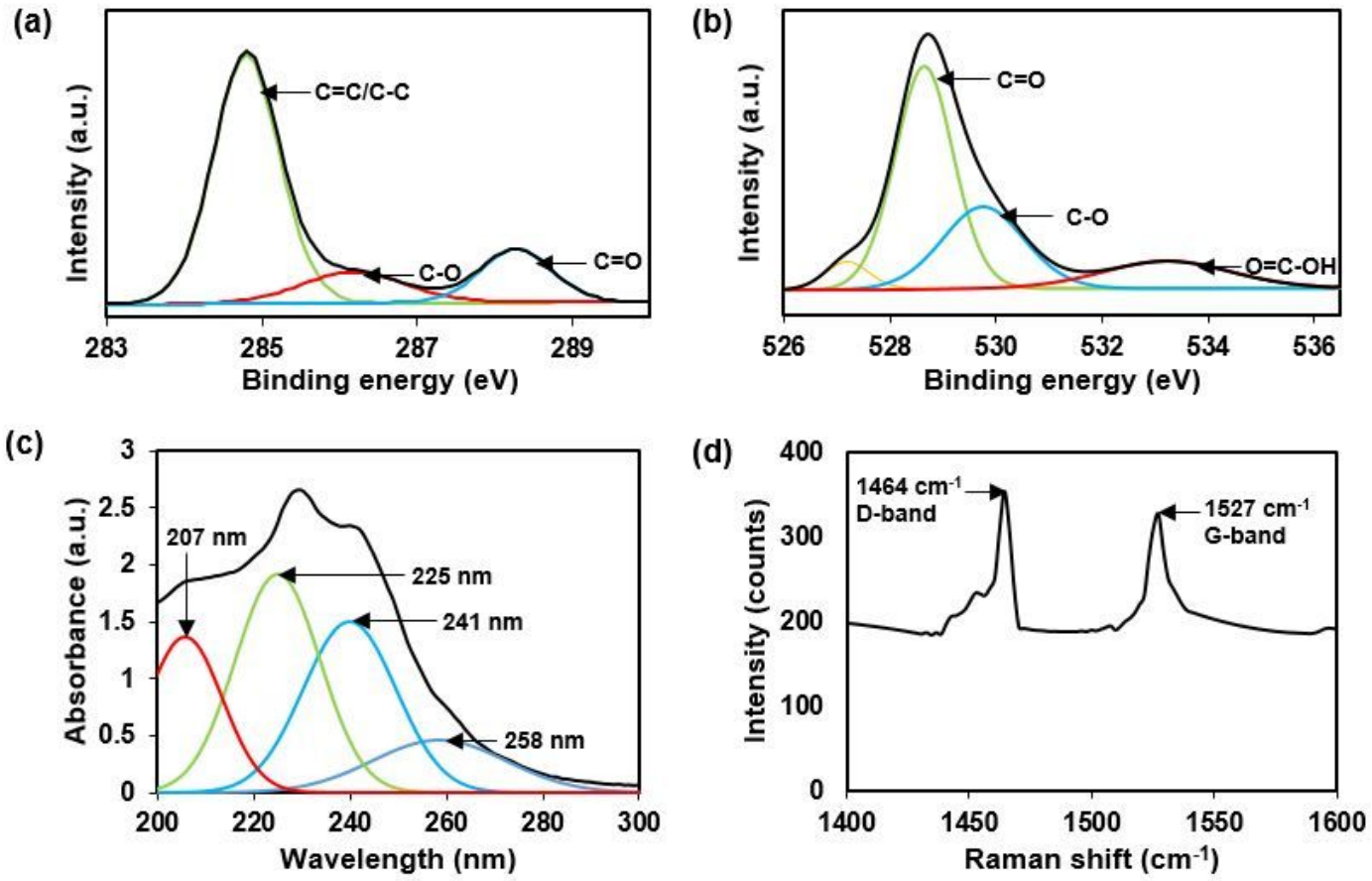

Figure 4

GQDs XPS spectra of (a) C1s and (b) O1s, (c) absorbance of GQDs, and (d) Raman spectrum of GQDs

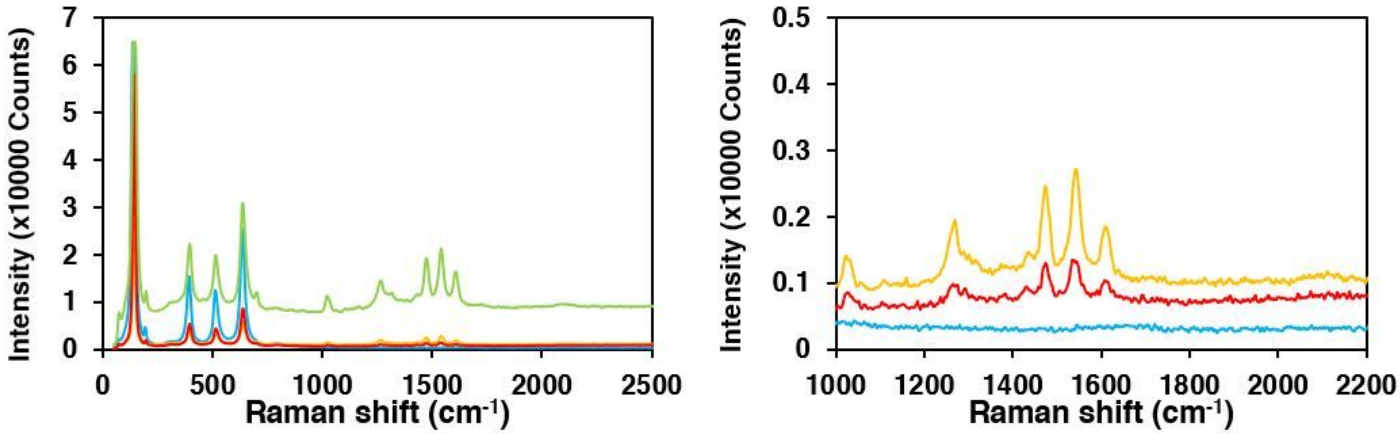

Figure 5

Raman spectra of TiO2, TiO2-N719, TiO2-mixture, and TiO2-LBL with (a) full-spectrum and (b) zoomed-in image of red region from graph (a) excluding TiO2 spectrum

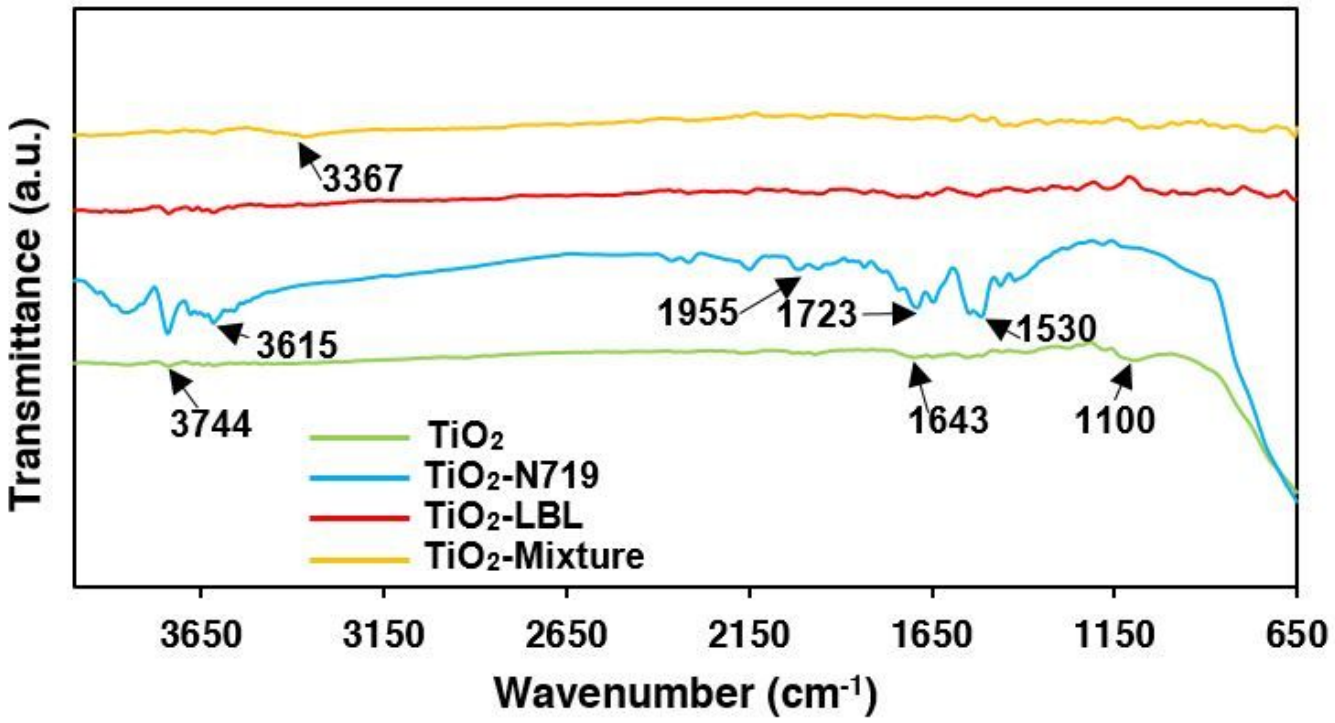

Figure 6

FTIR spectra of TiO2, TiO2-N719, TiO2-mixture, and TiO2-LBL

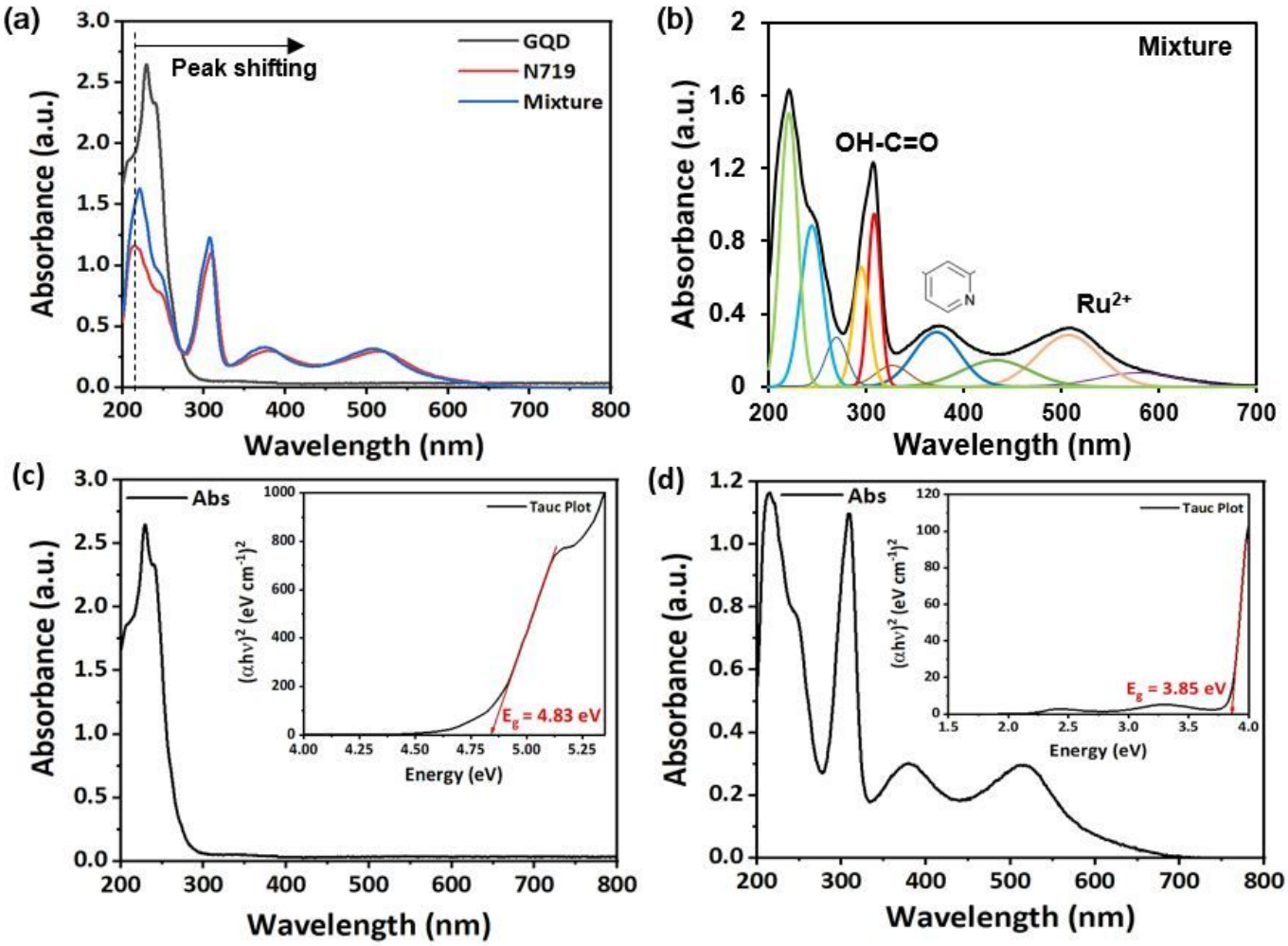

Figure 7

Absorbance of (a) peak fitting of GQDs, N719 and mixture solution, (b) peak deconvolution of mixture solution and Tauc plots of (c) GQD and (d) N719

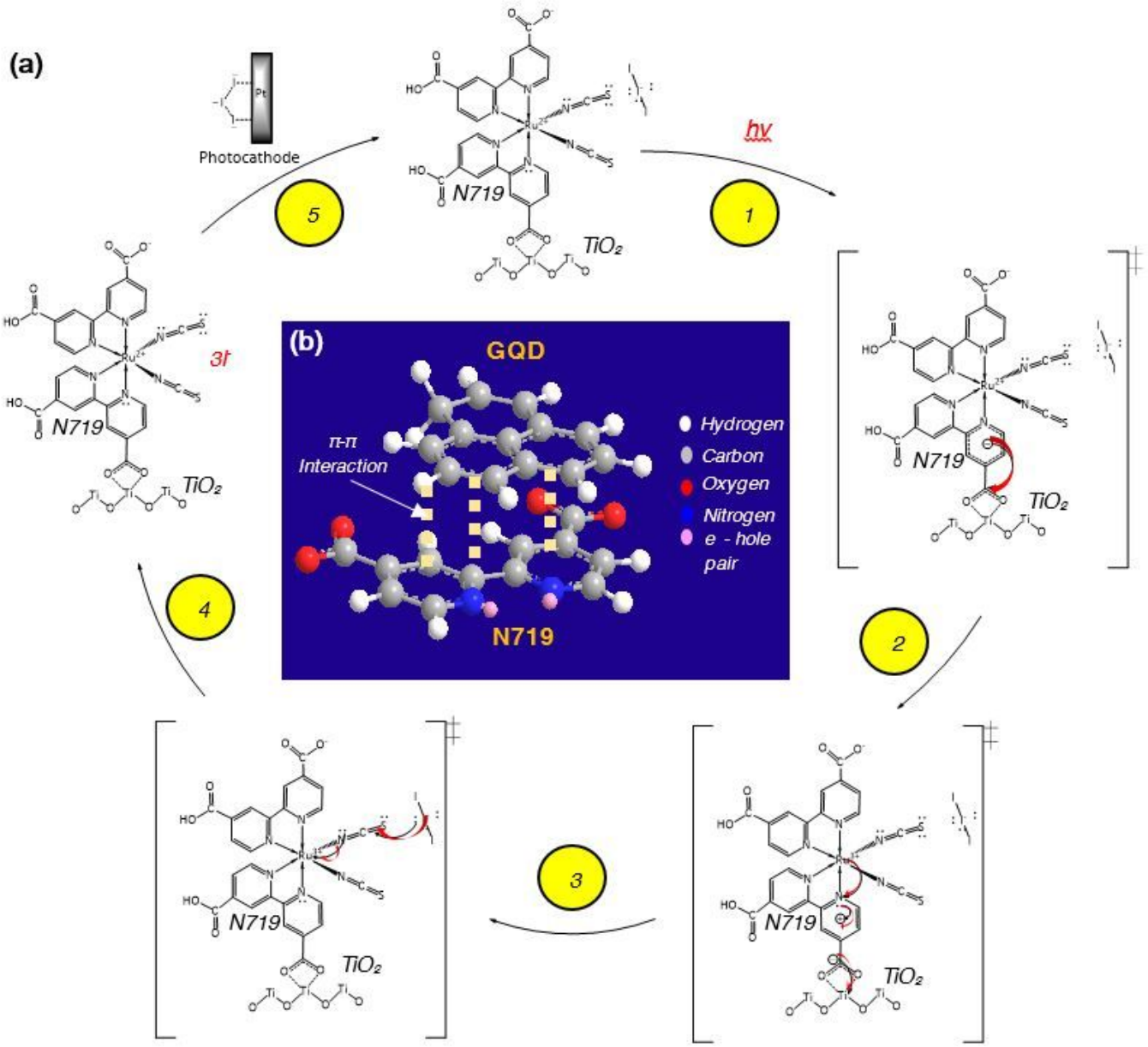

Figure 8

Illustration of (a) interaction among TiO2, N719, and triiodide molecules, and (b) π-π interaction between GQDs and bipyridine group of N719

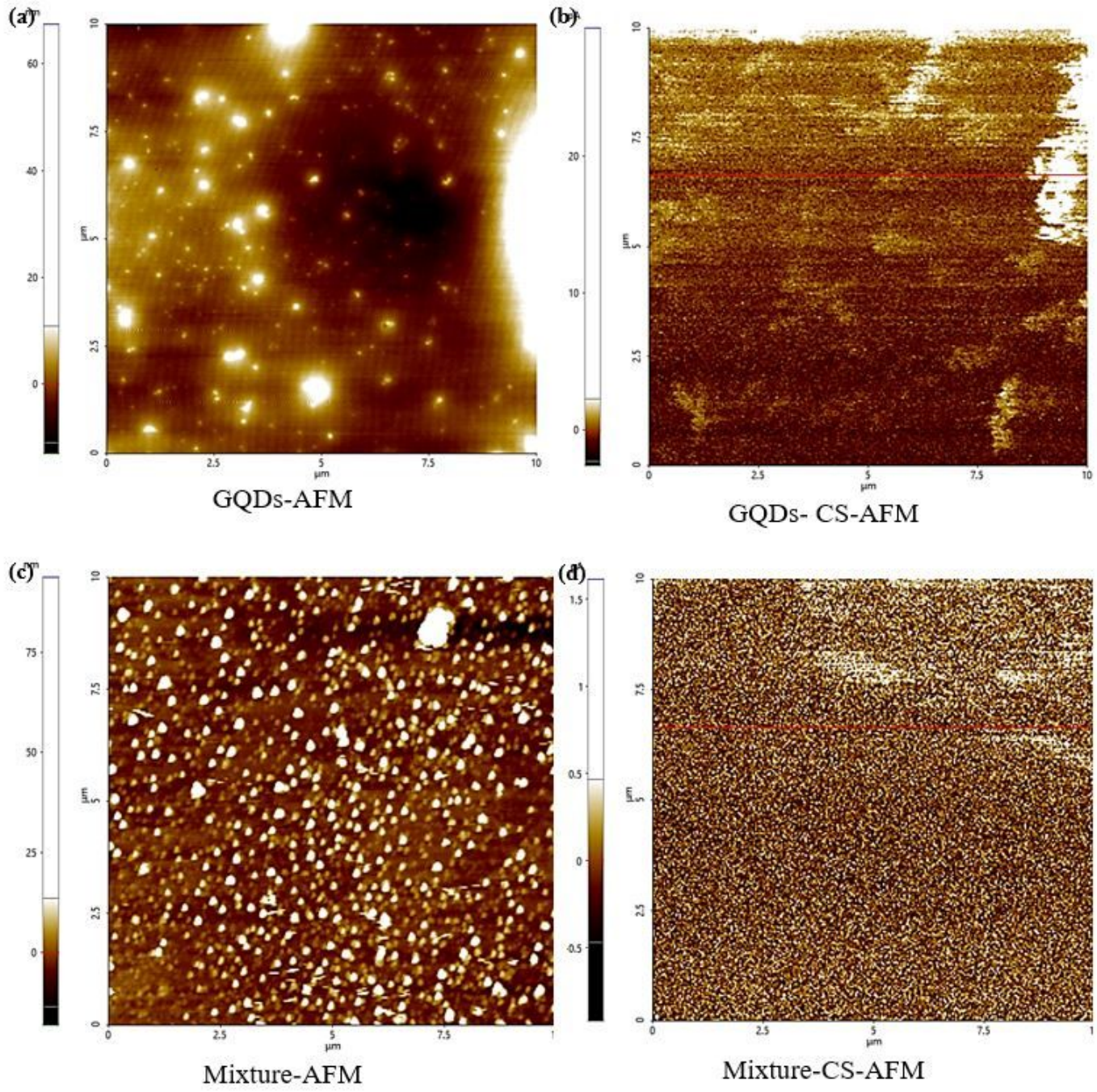

Figure 9

AFM topography of (a) GQDs and (c) mixture, and CS-AFM measurement of (b) GQDs and (d) mixture

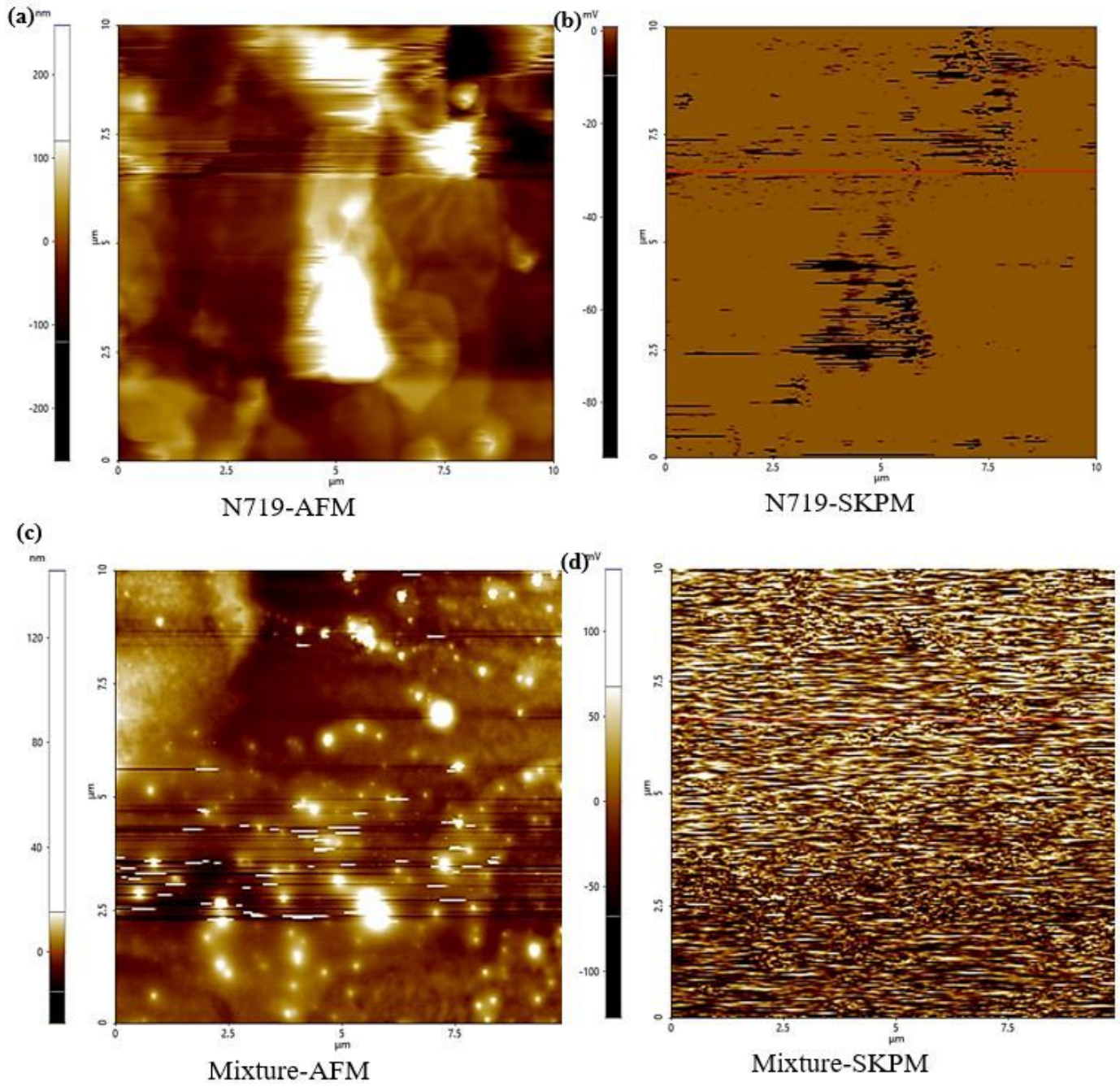

Figure 10

AFM topography of (a) N719 and (c) mixture, and SKPM measurement of (b) N719 and (d) mixture

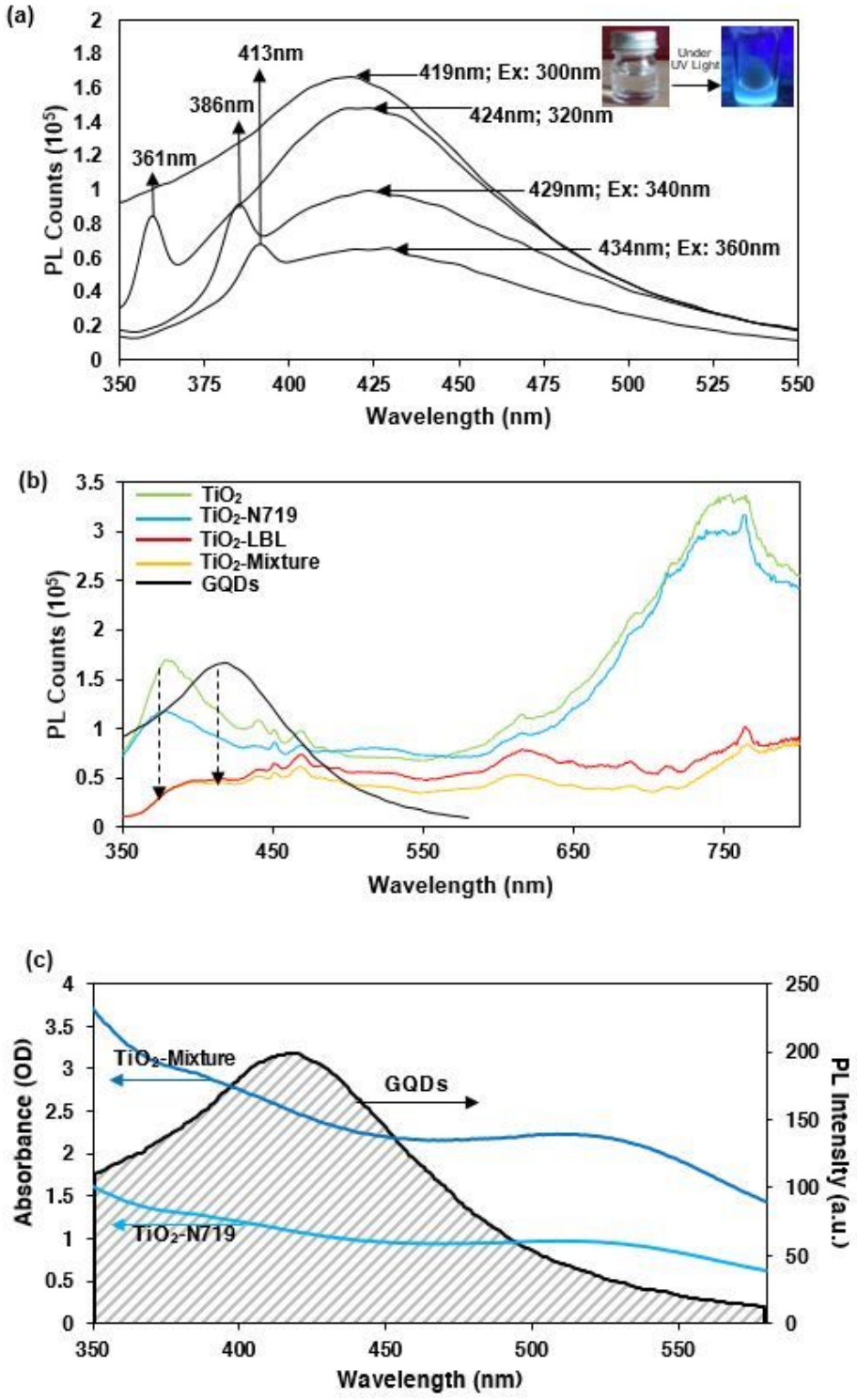

Figure 11

Photoluminescence of (a) GQDs, and (b) thin film samples and (c) absorbance of TiO2-mixture and TiO2-N719 and photoluminescence of GQDs to support FRET mechanism

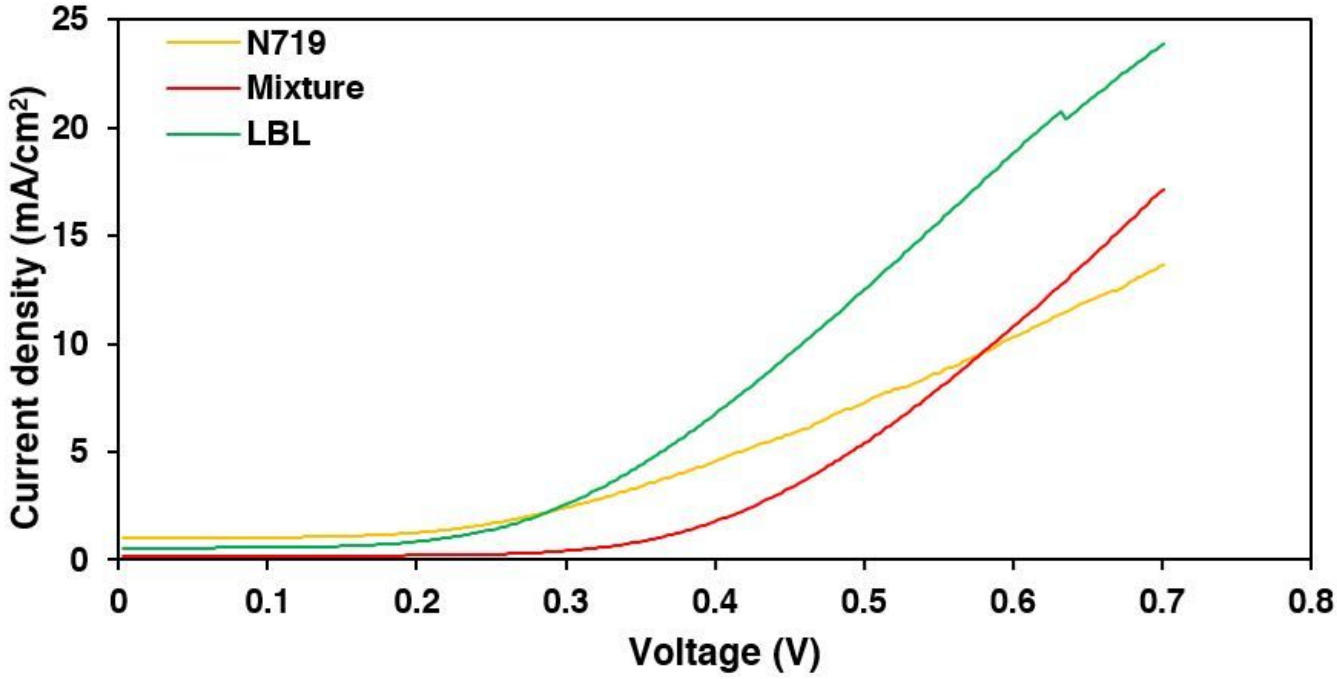

Figure 12

J-V curves measured under 0.5 mW/cm2 of low illumination for TiO2-DSSC sensitized with N719, mixture, and LBL

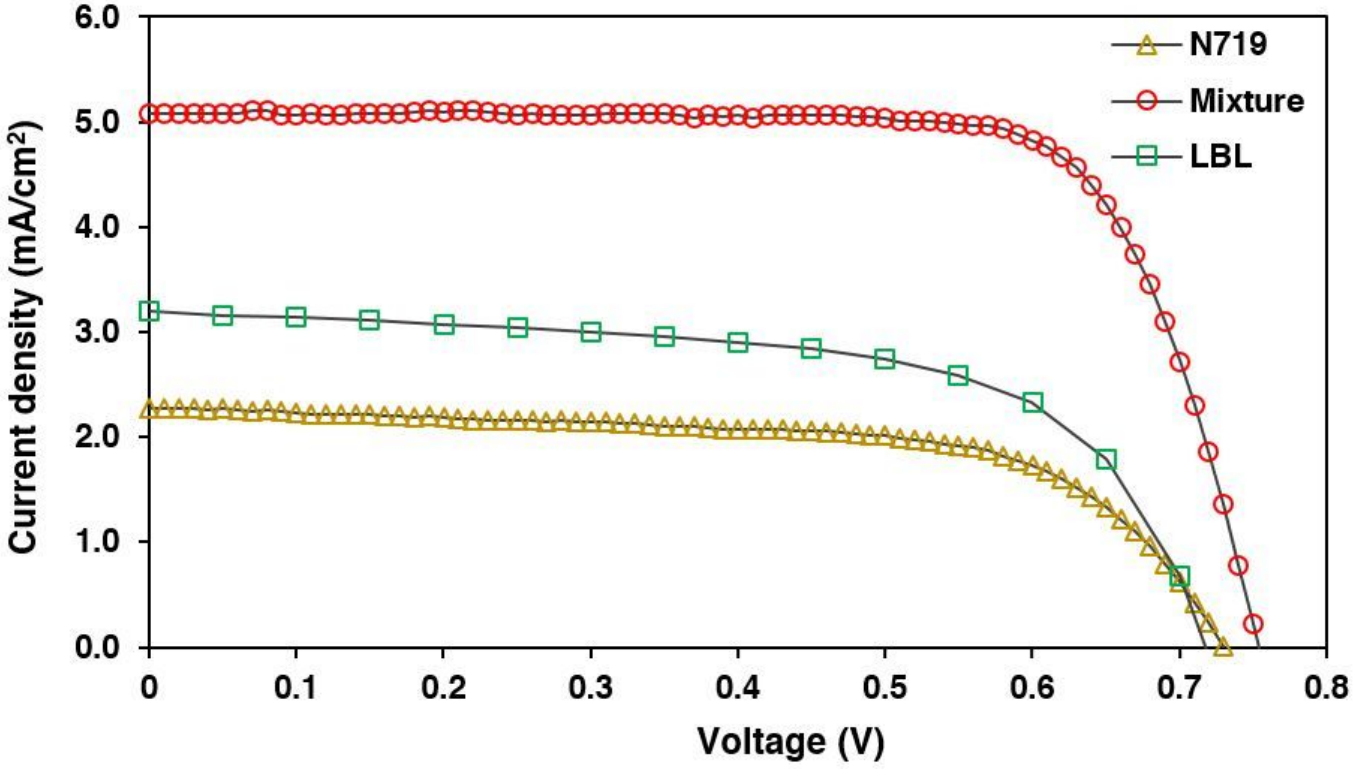

Figure 13

J-V curves under 100 mW/cm2 illumination for TiO2-DSSC sensitized with N719, mixture, and LBL

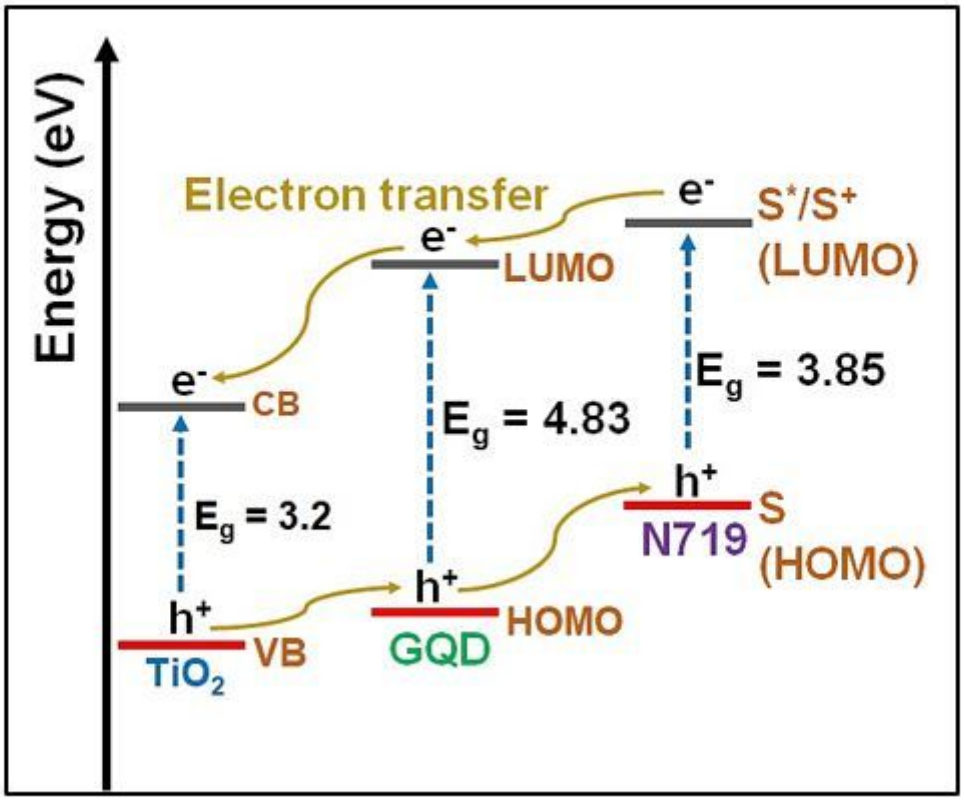

Figure 14

Energy band structure and electron mechanism in the TiO2-DSSC sensitized with GQD, and N719

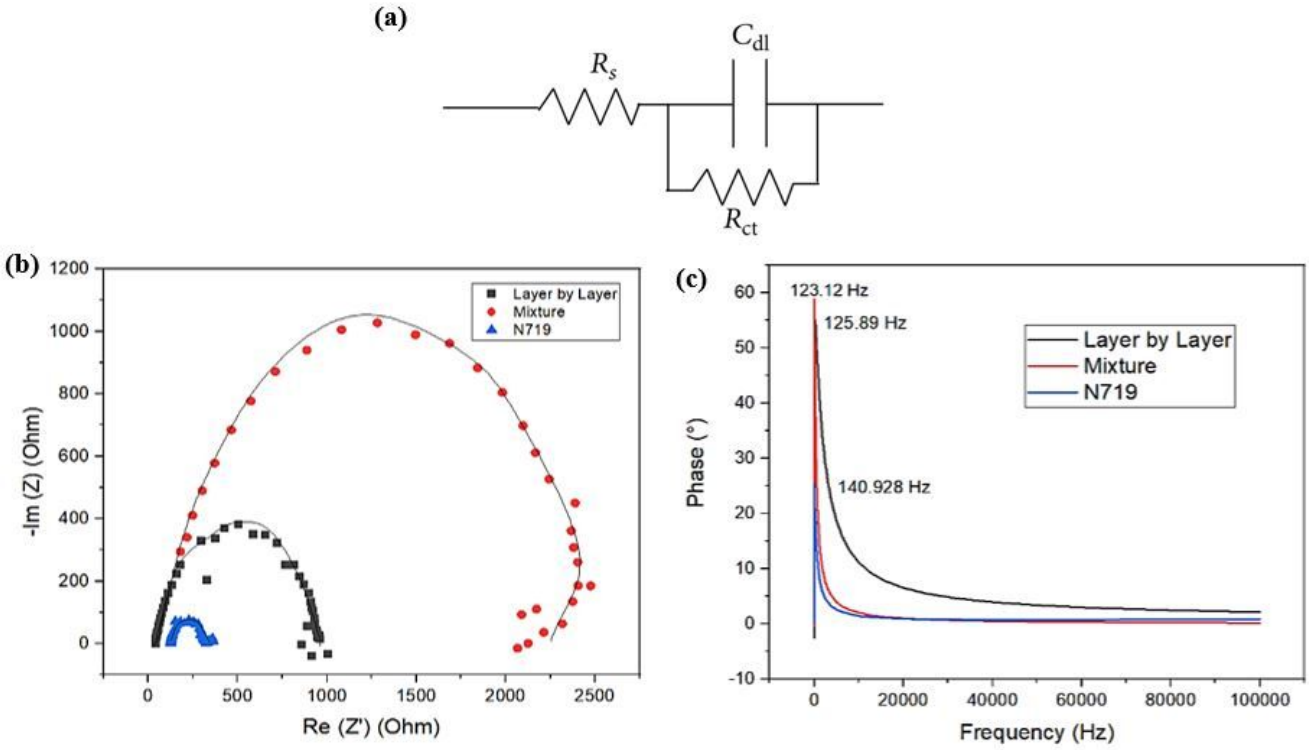

Figure 15

(a) A simple equivalent circuit, (b) fitted Nyquist plot and (c) Bode plot of TiO2-DSSC sensitized with N719, mixture, and LBL